Muon Interaction with Negative-*U* and High-Spin-State Defects: Differentiating Between C and Si Vacancies in 4*H*-SiC

J. Woerle,[1,*] M.E. Bathen,[2] T. Prokscha,[3] A. Galeckas,[2] H.M. Ayedh,[2] L. Vines,[2] and U. Grossner[1]

[1] *Advanced Power Semiconductor Laboratory, ETH Zurich, Physikstrasse 3, Zurich 8092, Switzerland*
[2] *Centre for Materials Science and Nanotechnology, Department of Physics, University of Oslo, Oslo N-0316, Norway*
[3] *Laboratory for Muon Spin Spectroscopy, Paul Scherrer Institute, Villigen 5232, Switzerland*

(Received 3 June 2020; revised 4 September 2020; accepted 22 October 2020; published 20 November 2020)

Low-energy muon-spin-rotation spectroscopy (LE-μSR) is employed to study silicon and carbon vacancies in proton-irradiated 4*H*-SiC. We show that the implanted muon is quickly attracted to the negative Si vacancy (V_{Si}), where it forms a paramagnetic muonium (Mu^0) state, resulting in a reduction of the diamagnetic fraction. In samples with predominantly C vacancies (V_C), on the other hand, the formation of Mu^0 is very short lived and the muon quickly captures a second electron to form a diamagnetic Mu^- state. The results are corroborated by density-functional calculations, where significant differences in the relaxation mechanism of the nearest-neighbor dangling bonds of the vacancies are discussed. We propose that the LE-μSR technique is capable of differentiating between high-spin and negative-*U* behavior in semiconducting materials. Finally, our findings emphasize the large potential of LE-μSR to probe near-surface semiconductor defects, a capability that is crucial for further development of many electronic and quantum technology applications.

DOI: 10.1103/PhysRevApplied.14.054053

I. INTRODUCTION

Vacancy defects are a fundamental aspect of solids, frequently altering the electronic and optical properties of materials. In silicon carbide (SiC), a semiconductor material that shows promise for both power-electronics and quantum technology applications, slight differences in electronegativity between the two atomic species have profound implications for the effect of a specific vacancy on the electronic properties of the material at large.

Silicon carbide is considered a covalent material, in which Si and C form a strong bond. At the same time, there is also a distinct ionic contribution to the bonding, where C is the negatively charged constituent. Consequently, SiC embodies two vacancy types, silicon and carbon vacancies (V_{Si} and V_C, respectively), with significantly different behavior. V_C is surrounded by Si atoms having extended dangling bonds that overlap and the degenerate ground state makes V_C susceptible to a symmetry-lowering Jahn-Teller (JT) distortion [1–5]. In epitaxially grown 4*H*-SiC, V_C has been identified as a lifetime-killing defect, thereby lowering the performance of 4*H*-SiC power-electronic devices [6]. Furthermore, V_C is associated with a negative-*U* behavior, which manifests in the $(-/2-)$ charge-state transition of V_C taking place at higher energies than $V_C(0/-)$ [7]. V_{Si}, on the other hand, is surrounded by highly localized C orbitals with negligible overlap, similar to the vacancy in diamond. Without nearest-neighbor bonding, there is no driving force for a JT distortion in $V_{Si}$and an inward displacement is only achieved at a high energetic cost. Instead, the Si-C bonds shorten, yielding a symmetry-conserving outward-breathing relaxation. Moreover, V_{Si}^- exhibits a spin of $S = 3/2$, long spin-coherence times, and single-photon emission [8], in contrast to the low-spin ($S = 0$) and negative-*U* character of V_C [7,9]. Owing to these properties, the V_{Si} has been identified as a promising candidate for a wide range of quantum applications, including quantum communication, computing, and sensing [8,10,11].

There exists a range of techniques capable of detecting and identifying isolated point defects in SiC. In photoluminescence (PL) spectroscopy, the V_{Si} exhibits a well-known fingerprint [12,13] and using deep-level transient spectroscopy (DLTS), the (–/2–) and (2–/3–) charge-transition levels of V_{Si} [14] and the $(0/2-)$ transition of V_C [7] have been successfully identified. However, especially the top approximately 300 nm of a sample, i.e., wherein a qubit V_{Si} will likely reside, is difficult to analyze with the aforementioned methods. DLTS is most accurate starting from some hundreds of nanometers, depending on the nature of

*woerle@aps.ee.ethz.ch

the junction [15], and depth-resolved PL spectroscopy is challenging due to the difficulty in localizing light emitters.

Nondestructive particle-beam methods for defect detection include positron-annihilation spectroscopy (PAS) and muon-spin-rotation (μSR) spectroscopy. PAS is selectively sensitive to vacancylike defect concentrations in the range from 1×10^{15} cm^{-3} to 1×10^{19} cm^{-3} [16]. Although probing depths in the submicron range are technically possible, most studies on SiC focus on defects deep in the bulk [17–19]. Low-energy μSR (LE-μSR) has been successfully used for the investigation of defect profiles near the surface [20,21] and has also been deployed to study band bending and charge-carrier profiles as well as their manipulation in semiconductors [22,23]. Recently, LE-μSR has also been demonstrated to detect carbon vacancies in the first 120 nm of irradiated *n*-type 4*H*-SiC [24]. Herein, we investigate the interaction of the muon with both V_{Si} and V_C in *n*-type 4*H*-SiC samples that are proton irradiated to varying fluences and compare experimental findings with density-functional theory (DFT) calculations using hydrogen as a substitute for the muon. We find a distinct difference in the response of the muons to the silicon and carbon vacancies, both using LE-μSR and DFT, and we propose that the LE-μSR technique is sensitive to the distinct relaxation mechanisms driven by the vacancy nearest-neighbor dangling bonds. Our results demonstrate that LE-μSR is a promising technique for detecting and identifying point defects in semiconductors in a nondestructive fashion, with the added benefit of gaining detailed information on the local magnetic environment of the defect.

II. METHODS

A. Sample preparation and characterization

In this study, proton-irradiated *n*-type 4*H*-SiC samples containing both V_{Si} and V_C defects are investigated. The samples studied are 10-μm-thick (0001) 4*H*-SiC epitaxial layers, grown 4° off the *c* axis on a 4*H*-SiC substrate (CREE). The net carrier concentration in the epilayers is approximately $N_D = 10^{15}$ cm^{-3} as determined from capacitance-voltage measurements, while the substrate *n*-type doping is reported to be approximately 8×10^{18} cm^{-3}. To generate the Si and C vacancies, the samples are irradiated at room temperature to different fluences with 1.8-MeV protons and at an angle 8° off the surface normal to reduce channeling effects. According to Monte Carlo simulations (as implemented in the stopping and range of ions in matter (SRIM) code [25]), the projected range of the protons is approximately 27 μm. A low-temperature annealing process ($T_{Anneal} = 300\,^{\circ}$C, 30 min, N_2 flow) is used to alleviate implantation damage and remove unstable defects, leaving predominantly V_{Si} and V_C with a ratio of approximately 0.6 [14] in the samples. Two additional samples, one with and one without a prior proton-irradiation step, receive a heat treatment at $T_{Anneal} = 1200\,^{\circ}$C (30 min, Ar atmosphere). In the case of the irradiated sample, the high-temperature heat treatment is conducted to reduce the concentration of silicon vacancies, leaving mainly V_C present in the sample. The nonirradiated reference sample is included to gauge the effect of the annealing process on the defect population. Hydrogen from the proton irradiation itself is not expected to be present in the near-surface region probed during the muon experiments. The sample-processing conditions and estimated V_{Si} and V_C concentrations in each sample, based on SRIM simulations and the DLTS-PL correlation methodology of Ref. [14], are summarized in Table I.

TABLE I. The sample-processing conditions and estimated V_{Si} and V_C concentrations (based on Ref. [14]) in the near-surface region of the 4*H*-SiC samples. The V_C concentration of the nonirradiated sample is determined using DLTS.

Fluence (cm^{-2})	T_{Anneal} (°C)	[V_{Si}] (cm^{-3})	[V_C] (cm^{-3})
1×10^{13}	300	3.0×10^{14}	5.0×10^{14}
4.5×10^{13}	300	1.4×10^{15}	2.3×10^{15}
1×10^{14}	300	3.1×10^{15}	5.2×10^{15}
3×10^{14}	300	9.3×10^{15}	1.5×10^{16}
None	1200	$\ll 5.0 \times 10^{12}$	5.0×10^{12}
4.5×10^{13}	1200	$\ll 3.0 \times 10^{14}$	$\sim 2 \times 10^{15}$

Deep-level transient spectroscopy (DLTS) measurements are performed on the nonirradiated reference sample to monitor any defects present in the as-grown material and to investigate whether additional defects are induced during the postirradiation annealing step ($T_{Anneal} = 1200\,^{\circ}$C). For the DLTS analysis, Ni Schottky-barrier diodes of 1 mm diameter and 150 nm thickness are deposited on the sample surface using an electron-beam evaporator. DLTS is performed in the temperature range from 25 K to 300 K to encompass both the S1 (related to V_{Si}) and $Z_{1/2}$ (related to V_C) peaks, along with any impurities arising close to the conduction-band edge. The reverse bias is kept at −10 V using a 10-V filling pulse, rate windows in the 20–640 ms range, and a standard lock-in weighting function to extract the DLTS signal.

To ascertain the presence and relative concentration of V_{Si} in the samples, additional photoluminescence (PL) measurements are conducted prior to the μSR analysis. Experiments are performed at 10 K, using a pulsed Ti:sapphire tunable laser at 740-nm excitation and a polarization perpendicular to the optical *c* axis of 4*H*-SiC to monitor V_{Si} signatures. To investigate the presence of divacancy ($V_{Si}V_C$) defects, a 405-nm excitation is employed using a cw laser of 75 mW power.

B. LE-μSR measurements

The μSR measurements are performed at the low-energy muon (LEM) beamline of the Swiss Muon Source

(SμS) [26,27]. Samples are fixed on a Ni-coated aluminum plate and mounted onto a cryostat placed perpendicular to the muon beam. A magnetic field is applied parallel to the beam axis and the positrons from the muon decay are detected by a set of scintillator detectors placed around the beam axis. The final kinetic energy of the μ^+ implanted into the sample is varied between 2 keV and 18.5 keV, resulting in probing depths up to 120 nm. Consequently, only near-surface defects in the proton-irradiation tail are probed. During a LE-μSR experiment, approximately 100% polarized positive muons are implanted into the 4H-SiC sample. After a short lifetime of approximately 2.2 μs, the μ^+ decays and emits a positron preferentially in the direction of its polarization at the time of the decay. Using an appropriate detector geometry, the asymmetry of the muon decay along different directions as a function of time, $A(t)$, which is proportional to the time evolution of the muon spin polarization, can be measured. $A(t)$ depends on the local electronic environment of the muon and can be used to obtain information on the hyperfine interaction between the muon and the electrons in the system. For more details on the μSR technique, see also Refs. [28–31].

C. Density-functional calculations

In addition to the experimental investigations, DFT calculations as implemented in the VASP code are performed [32–35]. The electronic ground state is obtained within the Kohn-Sham formalism, using the projector augmented-wave (PAW) method [36] to describe the core electrons, a 420-eV energy cutoff, and setting the stopping criterion for the electronic self-consistent loop to 10^{-6} eV. Muons are commonly not directly implemented in VASP but are instead emulated using the hydrogen pseudopotential [37,38]. Herein, we study interactions between muons and vacancies in 4H-SiC as represented by hydrogen-vacancy complexes (V_{Si}-H and V_{C}-H), from here on denoted as V_{Si}-Mu and V_{C}-Mu. In this context, Mu (one μ^+ bound to one e^-) corresponds to H consisting of one proton and one electron. Formation-energy diagrams for the defects are constructed according to Refs. [39,40] using the extended Freysoldt–Neugebauer–Van de Walle charge-correction scheme [41–43].

For the vacancy-Mu complexes, 400-atom hexagonal supercells are employed. Defect relaxation is conducted using the HSE06 [44,45] hybrid functional and Γ-only **k**-point sampling until the maximum force is below 0.05 eV/Å. Note that results for V_{Si}-H are based on that of Ref. [46].

In the case of isolated monovacancies, orthorombic 96-atom supercells and hybrid-derived lattice parameters (using HSE06) are employed. Here, one may discuss whether unintended defect-overlap effects may influence the results for defects situated within smaller 96-atom supercells. However, the supercells in question are near cubic, with approximately 10 Å between defects in all three dimensions, and hybrid-level relaxations are performed using a 2 × 2 × 2 Monkhorst–Pack-type **k** mesh.

III. RESULTS

A. Semiconductor bulk analysis

Before elaborating on the muon-beam analysis, we discuss the results of our DLTS and PL spectroscopy measurements used to estimate the defect populations in the 4H-SiC samples. In a first step, DLTS measurements are performed on the sample without proton irradiation to investigate the defect concentration already present in the epitaxial layer. As shown in Fig. 1(a), the $Z_{1/2}$ peak, related to the (0/2−) negative-U transition of the carbon vacancy [7] and commonly present in 4H-SiC epitaxial

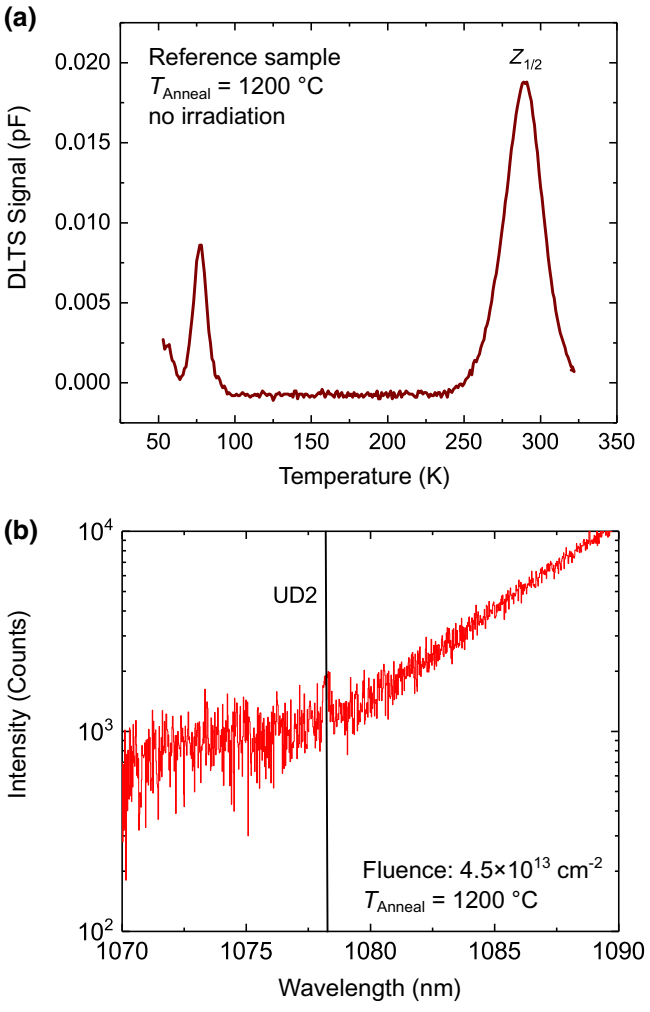

FIG. 1. (a) The DLTS spectrum using the 640-μs rate window for the nonirradiated reference sample. (b) The PL spectrum of a proton-irradiated 4H-SiC sample annealed at 1200 °C (fluence 4.5 × 10^{13} cm^{-2}), showing the UD2 signal related to the divacancy ($V_{\mathrm{Si}}V_{\mathrm{C}}$).

layers, is clearly observed. The measured peak intensity of $Z_{1/2}$ translates to a carbon-vacancy concentration of 5×10^{12} cm^{-3}. The second peak around 80 K is assigned to the cubic crystalline site of the nitrogen donor level [47] and is too small to play a significant role in the LE-μSR experiment. V_{Si}, on the other hand, is not detected in the prior to irradiation, as is apparent from the absence of the S1 peak near 200 K [14].

As the upper detection limit of DLTS is below approximately $0.2N_D$ and $N_D = 1 \times 10^{15}$ cm^{-3}, the irradiated samples cannot be studied using this technique. Instead, PL measurements are performed to investigate the presence of optically active defects such as V_{Si}, the divacancy ($V_{Si}V_C$), the carbon-antisite vacancy ($C_{Si}V_C$) pair, and the nitrogen-vacancy ($N_C V_{Si}$) center. The V_{Si} is clearly visible in all cases after irradiation, while neither the $C_{Si}V_C$ nor $N_C V_{Si}$ centers can be identified in any of the studied samples. Interestingly, in the irradiated sample that is annealed at 1200 °C, we observe a weak UD2 signal [Fig. 1(b)] that has previously been attributed to the divacancy [48]. Its appearance can be attributed to the increased annealing temperature at which V_{Si} becomes more mobile and hence facilitates the formation of the divacancy [49]. The annealing of the samples at 300 °C, on the other hand, is not sufficient to promote this mechanism.

For an estimation of the V_{Si} population, we monitor the V1/V1′ (at 1.44 eV) and V2 (at 1.35-eV) emission lines that are associated with the negative charge state of hexagonal (h) and pseudocubic (k) V_{Si}, respectively [13,50,51]. Emission from the proton-irradiated samples is shown in Fig. 2(a) for the wavelength range associated with V1/V1′. We find that the V_{Si} emission intensities increase with the proton fluence, as expected for the 300 °C-annealed samples [shown by the black line in Fig. 2(b)]. The V_{Si} is present also in the sample that is irradiated to a proton fluence of 4.5×10^{13} cm^{-2} and annealed at 1200 °C but in much lesser quantities [illustrated by the red dot and line in Fig. 2(b)]. The annealing of the V_{Si} above 300 °C happens by either outdiffusion or, as described before, by transformation into the divacancy.

Importantly, all the irradiated samples have defect concentrations close to or above N_D (see Table I) and hence are partly or fully compensated. For the lowest proton fluence (10^{13} cm^{-2}), the Fermi level likely resides somewhere between the (+/0) transition of V_C near midgap [9] and the (−/2−) transition of V_{Si} at 0.7 eV below the CBM [14,52], while for the higher-fluence samples the Fermi level will be pinned close to midgap by V_C(+/0). Consequently, for the present sample set, the equilibrium vacancy states are V_{Si}^- and V_C^0 (see, e.g., Refs. [9,14,52]).

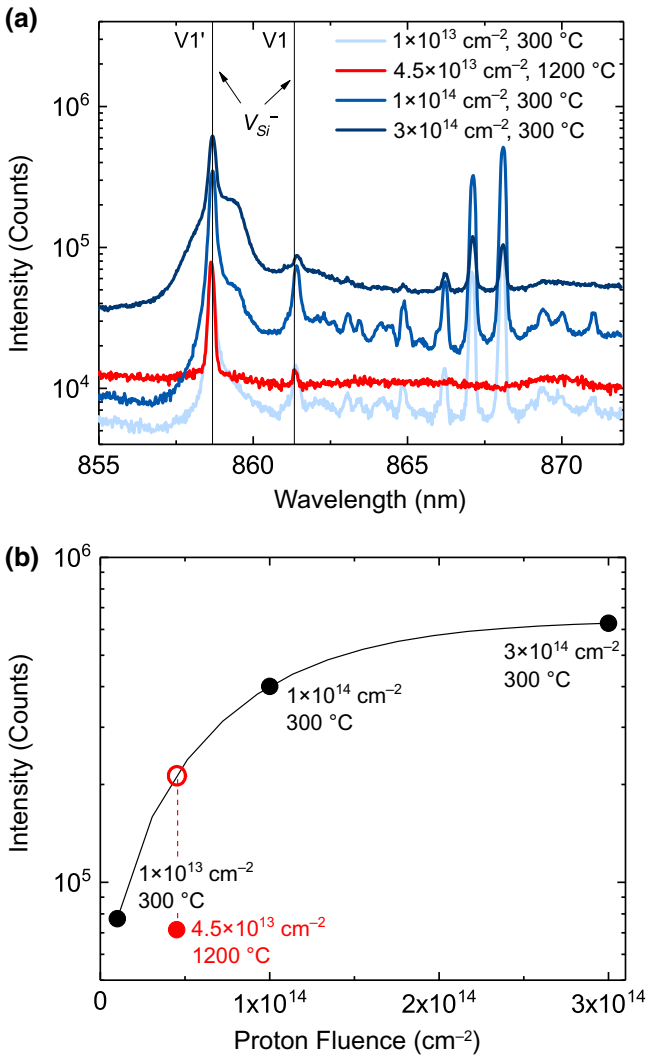

FIG. 2. The PL spectra of 4H-SiC samples irradiated to different fluences and annealed at 300 °C or 1200 °C, with (a) showcasing the V1/V1′ lines related to V_{Si} emission and (b) showing the background-subtracted V_{Si}-related emission intensities (V1+V1′+V2) versus the proton fluence. Annealing at 1200 °C results in a decrease of V_{Si}, indicated by the filled red circle.

B. LE-μSR analysis

When a μ^+ is implanted into a semiconductor during a μSR experiment, it stops at an interstitial site and forms the hydrogenlike bound state called muonium (Mu), which can occur in three different charge states: either as a neutral paramagnetic state Mu^0 (μ^+e^-) or as one of the two diamagnetic states Mu^- ($\mu^+e^-e^-$) or Mu^+ (μ^+). Having different precession frequencies in an external magnetic field, the paramagnetic and diamagnetic states can be spectroscopically distinguished and from the amplitudes of the corresponding precession signal the decay asymmetries A_{Mu} and A_D can be determined. Given knowledge of the total asymmetry $A_{tot} = A_D + 2A_{Mu}$, the diamagnetic fraction $F_D = A_D/A_{tot}$ and the paramagnetic fraction $F_{Mu} = 2A_{Mu}/A_{tot}$ can be extracted. The factor of 2 in $2A_{Mu}$ accounts for the fact that, in our experiments with a low

magnetic field (0.5 mT), only 50% of the Mu^0 polarization is visible in the Mu^0 precession signal.

The formation of paramagnetic Mu^0 inside the target material is closely connected to the deceleration process of the muon during the first picoseconds after its implantation. Once the muon has slowed down sufficiently and reaches energies of a few kiloelectronvolts to tens of electronvolts, a cyclic charge exchange between a positive and a neutral charge state arises. The muon can leave this region either as a positively charged Mu^+or as a neutral Mu^0 atom [53], which then thermalizes and stops at an interstitial site that is attributed to the tetrahedral silicon (T_{Si}) site [54,55]. In low-doped nonirradiated 4*H*-SiC, more than half of the implanted μ^+ thermalize as Mu^0 [54,56], while typical values for the diamagnetic fraction F_D are below 0.1 [57]. The remaining *missing* fraction is the fraction of implanted μ^+ that does not contribute to the measured asymmetry due to fast depolarization effects.

In Fig. 3, F_D and F_{Mu} are shown as a function of the muon implantation energy in a transverse magnetic field of 0.5 mT. For low implantation energies (< 10 keV), an increased diamagnetic fraction is observed for all samples [Fig. 3(a)], which can be explained by a partial suppression

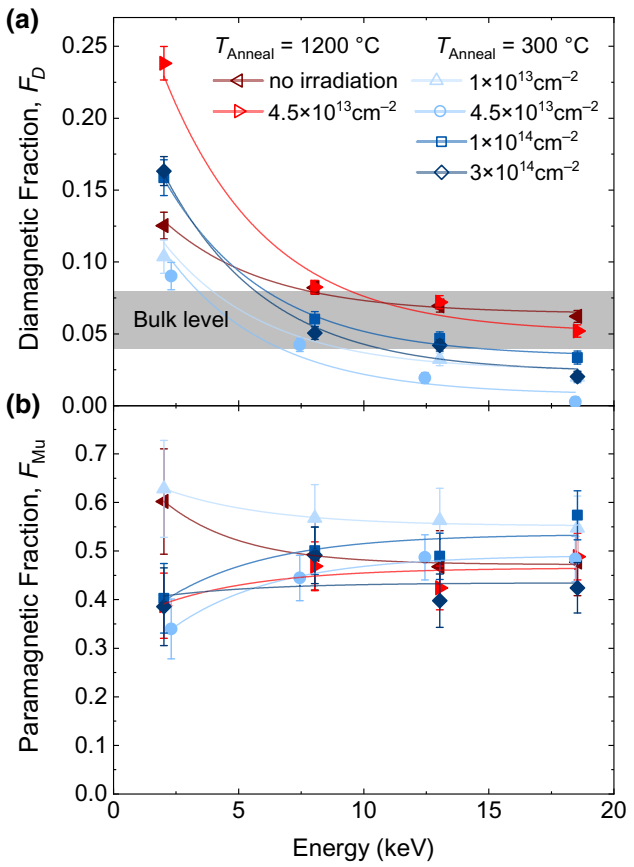

FIG. 3. The (a) diamagnetic and (b) paramagnetic fractions measured at 200 K and 0.5 mT. The lines are guides to the eyes.

of the Mu^0 formation process, previously described in Refs. [58,59]: while slowing down, a fraction of the implanted μ^+ may capture an electron from its own ionization track and form—with some delay—Mu^0 at one of the antibonding AB_C and AB_{Si} sites [55]. This delayed Mu^0 fraction cannot be observed directly and is only visible as an increase in F_D in the first few nanometers of the sample, where the number of electrons from the muon track is still insufficient for a transition from Mu^+ to Mu^0. In contrast, F_{Mu} in Fig. 3(b) exhibits only a weak energy dependence, indicating that the measured Mu^0 fraction is formed promptly: this fraction is from muons leaving the charge cycles as $Mu^0$and thermalizing as Mu^0, i.e., no track electrons are required for its formation. This fraction is relatively independent of the vacancy concentrations present in the samples.

At energies > 10 keV, where most of the implanted μ^+ are expected to form either prompt or delayed Mu^0, samples annealed at different temperatures show clear variations in F_D: for both samples with very small V_{Si} concentrations (annealing at 1200 °C), F_D decreases to expected bulk values, while all four samples with larger V_{Si} concentrations exhibit significantly smaller diamagnetic fractions, indicating that hardly any Mu^+ (or Mu^-) is formed. Importantly, the two samples irradiated to the same fluence of 4.5×10^{13} cm^{-2} but annealed at different temperatures exhibit a very different diamagnetic behavior, suggesting that their difference in V_{Si} concentration is the driving force behind the reduced F_D signal.

In Fig. 4, the results of F_D at 0.5 mT from Fig. 3 are compared with additional measurements at 10 mT. At larger implantation depths, no or only a weak field dependence of F_D is observed in the samples annealed at 300 °C containing larger V_{Si} concentrations [Figs. 4(a) and 4(b)], whereas it is much more pronounced in the 1200- °C-annealed samples [Fig. 4(c)]. Similar strong field dependencies have been reported in bulk-μSR studies of 4*H*-SiC [56,60], with clear indications for the presence of two diamagnetic species, (i.e., Mu^+ and Mu^-) and a fluctuation between the two via an intermediate Mu^0 state. Such behavior has also been discussed in the process of reaching the final muon configuration after its implantation: there, the muon comes first to rest in the unrelaxed host lattice and reaches its final configuration only via a paramagnetic transition state [53]. In the case of 4*H*-SiC with very small V_{Si} concentrations, the suggested fluctuation between $Mu^+$and Mu^-states might be a consequence of this transition sequence, involving the AB_{Si} and AB_C sites.

At larger V_{Si} concentrations [Figs. 4(a) and 4(b)], the decrease of F_D and the reduced field dependence suggests a different relaxation process: before reaching one of the *AB* sites, Mu^+ may be attracted to the negative V_{Si} center, where it captures one electron and forms the paramagnetic Mu^0 state. As a consequence, the diamagnetic signal drops

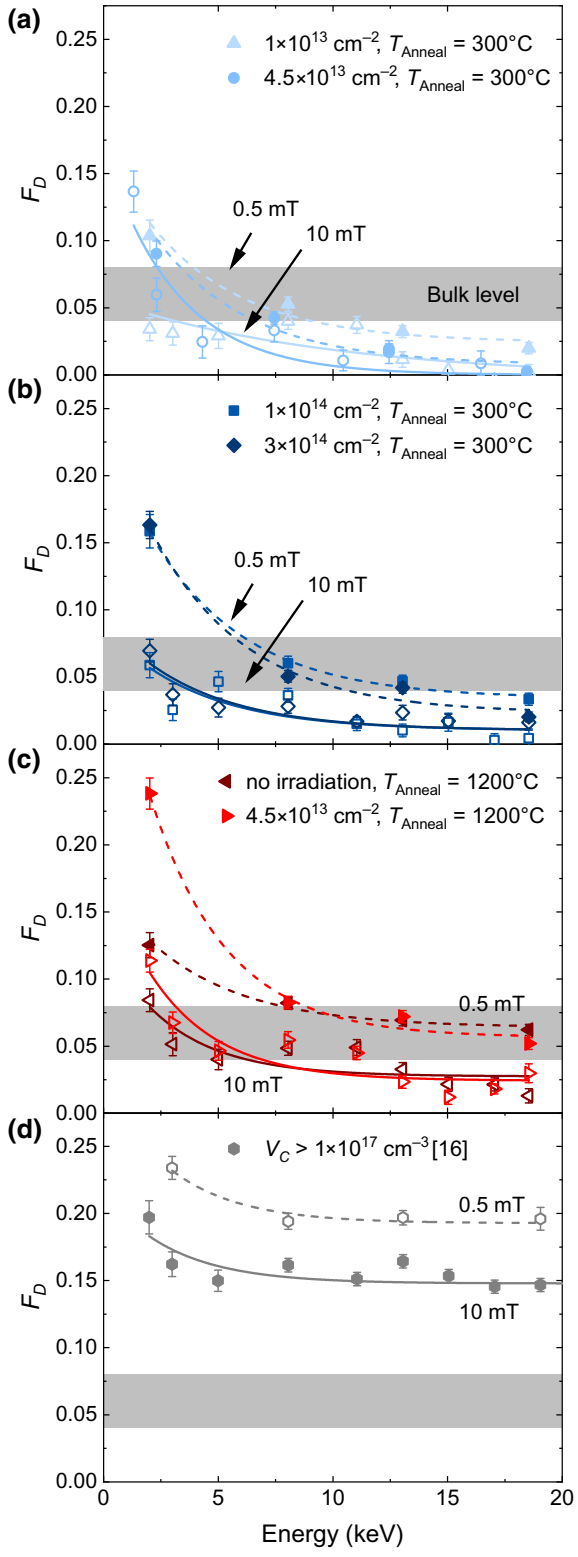

FIG. 4. The diamagnetic fractions measured at $B = 0.5$ mT (filled symbols) and $B = 10$ mT (empty symbols). (a),(b) Samples annealed at 300 °C, with increasing amounts of V_{Si} and V_C. (c) Samples annealed at 1200 °C and hence with negligible V_{Si} densities. (d) A proton-irradiated sample with a very large V_C and again a negligible V_{Si} concentration [24]. A field dependence, indicating a neutral precursor state, is most pronounced in the three samples in (c) and (d). The lines are guides to the eyes.

below the expected 4*H*-SiC bulk values and the field dependence is reduced.

In addition to the two discussed scenarios, it is interesting to compare our results with measurements on 4*H*-SiC with very large ($>10^{17}$ cm^{-13}) V_C and negligible V_{Si} concentrations [24], depicted in Fig. 4(d). Here, an increase of F_D and a decrease of F_{Mu} (not shown here) almost independent of the implantation energy is observed. In this case, the suppression of Mu^0 may be explained by (i) its trapping at V_C, where it captures an electron from the defect to form diamagnetic Mu^- or (ii) the capture of a Mu^+ at V_C, where a two-electron capture process leads first to the formation of $Mu^0$and finally to Mu^-.

C. DFT analysis

To better understand the muon dynamics in 4*H*-SiC, it is worthwhile to consider the different physical natures of V_{Si} and V_C, in terms of symmetry and local atomic displacement. Figures 5(a) and 5(c) demonstrate the contrast between the symmetry-conserving outward-breathing relaxation of V_{Si}^- [Fig. 5(a)], as compared to symmetry reduction and Si—Si dimer formation for V_C^0 [Fig. 5(c)]. Note the larger charge of V_{Si} compared to that of V_C for the same Fermi level and the larger void left by Si than for the V_C case.

To investigate the likelihood of the muon bonding to a vacancy and the stability of the resulting complex, we

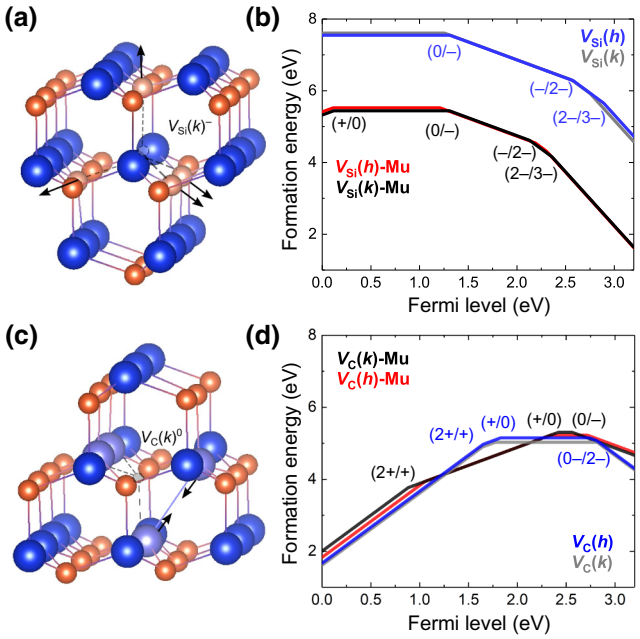

FIG. 5. Atomic structure and formation-energy diagrams for *h* and *k* for (a) V_{Si} and (b) V_{Si} and V_{Si}-Mu, and (c) V_C and (d) V_C and V_C-Mu. Si atoms are in blue or light blue (if distorted by the vacancy) and C atoms in orange or light orange. The total energies of V_{Si} are from Ref. [14] and those of V_{Si}-Mu are from Ref. [46]. The valence-band energy is offset to zero.

turn to formation-energy diagrams. Here, we can gauge the relative stability of the vacancies (V_{Si} and V_C) and vacancy-muon complexes (V_{Si} -Mu and V_C-Mu) for different Fermi levels. Formation-energy diagrams for V_{Si}-Mu and V_{Si}, and for V_C-Mu and V_C, are shown in Figs. 5(b) and 5(d), respectively. Similar to a previous study, we derive that V_{Si}-Mu is energetically more favorable than isolated V_{Si} [see Fig. 5(b)]. Consequently, if both constituents are available and in close proximity, the complex is likely to form. In contrast, we find that the formation energies for V_C and V_C-Mu are not significantly different, as shown in Fig. 5(d). This may imply that the trapping of the muon into V_C is less efficient than in the case of V_{Si}, as the energy gain from the muon binding to the V_C is lower than the gain from a V_{Si}-Mu formation for all Fermi levels. Upon considering the V_C and V_C-Mu formation-energy diagrams, we conclude that V_C is more stable than V_C-Mu for Fermi levels close to the conduction band, while the opposite is true for Fermi levels close to midgap. Hence, the rate of muon capture by V_C is significantly impacted by the Fermi levels in the samples and, as discussed above, the compensation of donors in our samples likely pushes the Fermi level toward midgap. Accordingly, trapping of muons by the V_C should be possible but is less likely than muon trapping by the V_{Si}.

To verify the electron-capture mechanisms predicted for μ^+, with the direct formation of the paramagnetic Mu^0 state at V_{Si} involving one electron, and a delayed two-electron capture at V_C, a Bader charge analysis [61–64] is performed. Overall, the electron cloud is found to locate predominantly around the C atoms, avoiding Si altogether. Upon considering the charge density surrounding the V_C-Mu and V_{Si}-Mu complexes for Fermi levels located both near midgap and close to CBM, we find a consistent trend: for the V_C-Mu complex, two electrons are located close to the muon, whereas a muon bound to V_{Si} will only attach to one electron, in accordance with the interpretation of the experimental data.

IV. DISCUSSION

An intriguing aspect of our findings that evolves when comparing the present results to a previous 4*H*-SiC study in Ref. [24] is the subject of sensitivity. Indeed, the muons appear to be far more sensitive to some defects than others, which highlights the need for a thorough understanding of the interplay between muons and different defect types. While a change in the μSR signal (i.e., a reduction of F_D) is already observed at V_{Si} concentrations around 3×10^{14} cm^{-3}, this is not the case for comparable V_C densities and the two samples annealed at 1200 °C exhibit very similar behavior despite their different V_C concentrations [Fig. 3(a)]. In short, we observe a much higher sensitivity of the muons toward V_{Si} than V_C. Based on the DFT calculations, this may be attributed to the greater charge of V_{Si} compared to V_C, providing a larger attractive Coulomb force for the positive muon, and a larger energy gain by V_{Si}-Mu complex formation compared to that of V_C-Mu (see Fig. 5). In addition, there are also structural differences between the two vacancies: as the void left by the Si atom is much larger than in the case of the V_C, the implanted muon may preferably stop at the more extended V_{Si}.

From our results, it is interesting to consider the close resemblance of the mechanisms for muon capture by V_{Si} and $V_C$and their fundamental properties as either high-spin or negative-*U* defects. A μ^+ in the vicinity of V_{Si} is captured to form an isolated and stable Mu^0, which does not interact further with the environment. This is similar to electron localization in V_{Si}^-, where weak interactions between V_{Si} and the surroundings result in long spin-coherence times and a weak outward-breathing motion of the neighboring carbon atoms. Conversely, the neighboring atoms surrounding V_C collapse inward following a symmetry-lowering path, leaving a smaller lattice void for the muon to fill in V_C compared to V_{Si}. The capture of μ^+ at V_C may also result in the formation of Mu^0 but interactions between V_C and the environment are strong, prompting the capture of a second electron and the formation of delayed Mu^-. In other words, the strong electron-phonon coupling of V_C leads to a prominent Jahn-Teller distortion of the surrounding geometry, which may be indirectly probed via the Mu formation process of the implanted μ^+. This interpretation is also supported by DFT calculations, where the geometric relaxation surrounding $(V_{Si}\text{-Mu})^-$ is almost identical to that of V_{Si}^-, while introducing a muon into V_C^0 and forming $(V_C\text{-Mu})^+$ yields significant interactions between μ^+ and the lattice. For Fermi levels approaching the CBM, the V_{Si} and V_C would take the charge states 3− and 2−, respectively, while retaining their distinct relaxation characteristics. Thus, the different muon-capture mechanisms by V_{Si} and V_C can be directly related to their proclivity toward either localized high-spin states or JT distortions.

V. CONCLUSION

In conclusion, the sensitivity of μ^+ to both V_{Si} and V_C with their distinct symmetry properties is successfully demonstrated. In the LE-μSR measurements performed on proton-irradiated 4*H*-SiC, it is revealed that V_{Si} concentrations as low as 3×10^{14} cm^{-3} already cause a reduction of F_D accompanied by a weakening of the field dependence. This is explained by the tendency of the Mu^+ to be trapped by V_{Si} and to capture one electron to form Mu^0. An effect on the μSR signal in the case of V_C is only observed at considerably larger concentrations ($>10^{17}$ cm^{-3}), where a suppression of promptly formed Mu^0 causes a strong increase of F_D. There, a two-electron capture process at the V_C needs to be considered, where a Mu^+ forms Mu^- via a short-lived Mu^0 state [24].

We propose that the LE-μSR technique is sensitive to the distinct relaxation mechanisms driven by the vacancy nearest-neighbor dangling bonds, based on the muon experiments and supporting DFT calculations. Jahn-Teller distortions are often characteristics of negative-U defects [65] such as V_C in SiC and the Si vacancy in silicon, while weak relaxations due to small electron-phonon interactions are commonly found for qubit candidates such as V_{Si} in SiC and the N-V center in diamond [66,67]. Consequently, the muon technique may also be used to differentiate between high-spin and negative-U behavior for systems besides SiC, e.g., in SiGe, where negative-U behavior and JT distortions are predicted for the Ge vacancy, while the Si vacancy exhibits high-spin qubit capabilities [68]. Our results also emphasize the large potential of LE-μSR to identify and distinguish defects close to the semiconductor surface, which is a key aspect for many electronic and quantum technology applications.

ACKNOWLEDGMENTS

The muon measurements were performed at the Swiss Muon Source SμS, Paul Scherrer Institute, Villigen, Switzerland. Special thanks go to the HIPA team for providing a stable primary proton beam. Financial support was kindly provided by the Research Council of Norway and the University of Oslo through the frontier research project Functionalizing Defects in Advanced Semiconductors (FUNDAMeNT) (Grant No. 251131, FriPro ToppForsk-program). The Research Council of Norway is acknowledged for the support to the Norwegian Micro- and Nano-Fabrication Facility, NorFab, Project No. 245963. The computations were performed on resources provided by UNINETT Sigma2—the National Infrastructure for High Performance Computing and Data Storage in Norway.

[1] F. Bechstedt, A. Zywietz, and J. Furthmüller, Carbon vacancy in SiC: A negative-U system, Europhys. Lett. **44**, 309 (1998).

[2] J. Furthmüller, A. Zywietz, and F. Bechstedt, Monovacancies in 3C and 4H SiC, Mater. Sci. Eng. **B61–62**, 244 (1999).

[3] A. Zywietz, J. Furthmüller, and F. Bechstedt, Vacancies in SiC: Influence of Jahn-Teller distortions, spin effects, and crystal structure, Phys. Rev. B **59**, 15166 (1999).

[4] A. Zywietz, J. Furthmüller, and F. Bechstedt, Intravacancy transition energies in 3C- and 4H-SiC, Phys. Rev. B **61**, 13655 (2000).

[5] A. Zywietz, J. Furthmüller, and F. Bechstedt, Spin state of vacancies: From magnetic Jahn-Teller distortions to multiplets, Phys. Rev. B **62**, 6854 (2000).

[6] T. Kimoto, Lifetime-killing defects in 4H-SiC epilayers and lifetime, Phys. Status Solidi B: Basic Solid State Phys. **245**, 1327 (2008).

[7] N. T. Son, X. T. Trinh, L. S. Løvlie, B. G. Svensson, K. Kawahara, J. Suda, T. Kimoto, T. Umeda, J. Isoya, T. Makino, T. Ohshima, and E. Janzén, Negative-U System of Carbon Vacancy in 4H-SiC, Phys. Rev. Lett. **109**, 187603 (2012).

[8] M. Widmann, S.-Y. Lee, T. Rendler, N. T. Son, H. Fedder, S. Paik, L.-P. Yang, N. Zhao, S. Yang, I. Booker, A. Denisenko, M. Jamali, S. A. Momenzadeh, I. Gerhardt, T. Ohshima, A. Gali, E. Janzén, and J. Wrachtrup, Coherent control of single spins in silicon carbide at room temperature, Nat. Mater. **14**, 164 (2014).

[9] Theory of the carbon vacancy in 4H-SiC: Crystal field and pseudo–Jahn-Teller effects, Phys. Rev. B **96**, 174105 (2017).

[10] S. Castelletto, L. Rosa, and B. C. Johnson, in *Advanced Silicon Carbide Devices and Processing* (InTech, London, 2015).

[11] H. Kraus, V. A. Soltamov, D. Riedel, S. Väth, F. Fuchs, A. Sperlich, P. G. Baranov, V. Dyakonov, and G. V. Astakhov, Room-temperature quantum microwave emitters based on spin defects in silicon carbide, Nat. Phys. **10**, 157 (2014).

[12] E. Sörman, N. T. Son, W. M. Chen, O. Kordina, C. Hallin, and E. Janzén, Silicon vacancy related defect in 4H and 6H SiC, Phys. Rev. B **61**, 2613 (2000).

[13] M. Wagner, B. Magnusson, W. M. Chen, E. Janzén, E. Sörman, C. Hallin, and J. L. Lindström, Electronic structure of the neutral silicon vacancy in 4H and 6H SiC, Phys. Rev. B **62**, 16555 (2000).

[14] M. E. Bathen, J. Coutinho, H. M. Ayedh, J. Ul Hassan, I. Farkas, S. Öberg, Y. K. Frodason, B. G. Svensson, and L. Vines, Anisotropic and plane-selective migration of the carbon vacancy in SiC: Theory and experiment, Phys. Rev. B **100**, 014103 (2019).

[15] H. M. Ayedh, A. Hallén, and B. G. Svensson, Elimination of carbon vacancies in 4H-SiC epi-layers by near-surface ion implantation: Influence of the ion species, J. Appl. Phys. **118**, 175701 (2015).

[16] Filip Tuomisto and Ilja Makkonen, Defect identification in semiconductors with positron annihilation: Experiment and theory, Rev. Mod. Phys. **85**, 1583 (2013).

[17] A. A. Rempel, W. Sprengel, K. Blaurock, K. J. Reichle, J. Major, and H.-E. Schaefer, Identification of Lattice Vacancies on the Two Sublattices of SiC, Phys. Rev. Lett. **89**, 185501 (2002).

[18] Q. Xu, T. Yoshiie, and M. Okada, Positron annihilation of vacancy-type defects in neutron-irradiated 4H-SiC, J. Nuclear Mater. **386–388**, 169 (2009), Fusion Reactor Materials.

[19] J. Wiktor, X. Kerbiriou, G. Jomard, S. Esnouf, M.-F. Barthe, and M. Bertolus, Positron annihilation spectroscopy investigation of vacancy clusters in silicon carbide: Combining experiments and electronic structure calculations, Phys. Rev. B **89**, 155203 (2014).

[20] H. V. Alberto, R. C. Vilão, R. B. L. Vieira, J. M. Gil, A. Weidinger, M. G. Sousa, J. P. Teixeira, A. F. da Cunha, J. P. Leitão, P. M. P. Salomé, P. A. Fernandes, T. Törndahl, T. Prokscha, A. Suter, and Z. Salman, Slow-muon study of quaternary solar-cell materials: Single layers and p-n junctions, Phys. Rev. Mater. **2**, 025402 (2018).

[21] A. F. A. Simões, H. V. Alberto, R. C. Vilão, J. M. Gil, J. M. V. Cunha, M. A. Curado, P. M. P. Salomé, T. Prokscha,

A. Suter, and Z. Salman, Muon implantation experiments in films: Obtaining depth-resolved information, Rev. Sci. Instrum. **91**, 023906 (2020).

[22] T. Prokscha, H. Luetkens, E. Morenzoni, G. J. Nieuwenhuys, A. Suter, M. Döbeli, M. Horisberger, and E. Pomjakushina, Depth dependence of the ionization energy of shallow hydrogen states in ZnO and CdS, Phys. Rev. B **90**, 235303 (2014).

[23] T. Prokscha, K.-H. Chow, Z. Salman, E. Stilp, and A. Suter, Direct Observation of Hole Carrier-Density Profiles and Their Light-Induced Manipulation at the Surface of Ge, Phys. Rev. Appl. **14**, 014098 (2020).

[24] J. Woerle, T. Prokscha, A. Hallén, and U. Grossner, Interaction of low-energy muon with defect profiles in proton-irradiated Si and 4*H*-SiC, Phys. Rev. B **100**, 115202 (2019).

[25] J. F. Ziegler, M. D. Ziegler, and J. P. Biersack, SRIM—the stopping and range of ions in matter, Nuclear Instrum. Methods Phys. Res. Sect. B **268**, 1818 (2010).

[26] T. Prokscha, E. Morenzoni, K. Deiters, F. Foroughi, D. George, R. Kobler, A. Suter, and V. Vrankovic, The new muE4 beam at PSI: A hybrid-type large acceptance channel for the generation of a high intensity surface-muon beam, Nuclear Instrum. Methods Phys. Res. Sect. A **595**, 317 (2008).

[27] E. Morenzoni, H. Glückler, T. Prokscha, H. P. Weber, E. M. Forgan, T. J. Jackson, H. Luetkens, Ch. Niedermayer, M. Pleines, M. Birke, A. Hofer, J. Litterst, T. Riseman, and G. Schatz, Low-energy μSR at PSI: Present and future, Phys. B: Condens. Matter **289–290**, 653 (2000).

[28] R. F. Kiefl and T. L. Estle, in *Semiconductors and Semimetals*, edited by J. I. Pankove and N. M. Johnson (Elsevier, Amsterdam, 1991), Vol. 34, p. 547.

[29] S. J. Blundell, Spin-polarized muons in condensed matter physics, Contemp. Phys. **40**, 175 (1999).

[30] K. Nagamine, *Introductory Muon Science* (Cambridge University Press, Cambridge, 2003).

[31] P. Bakule and E. Morenzoni, Generation and applications of slow polarized muons, Contemp. Phys. **45**, 203 (2004).

[32] G. Kresse and J. Hafner, Ab initiomolecular dynamics for liquid metals, Phys. Rev. B **47**, 558 (1993).

[33] G. Kresse and J. Hafner, *Ab initio* molecular-dynamics simulation of the liquid-metal–amorphous-semiconductor transition in germanium, Phys. Rev. B **49**, 14251 (1994).

[34] G. Kresse and J. Furthmüller, Efficiency of *ab-initio* total energy calculations for metals and semiconductors using a plane-wave basis set, Comput. Mater. Sci. **6**, 15 (1996).

[35] G. Kresse and J. Furthmüller, Efficient iterative schemes for *ab initio* total-energy calculations using a plane-wave basis set, Phys. Rev. B **54**, 11169 (1996).

[36] P. E. Blöchl, Projector augmented-wave method, Phys. Rev. B **50**, 17953 (1994).

[37] F. Bernardini, P. Bonfá, S. Massidda, and R. de Renzi, *Ab initio* strategy for muon site assignment in wide band gap fluorides, Phys. Rev. B **87**, 115148 (2013).

[38] S. Sturniolo, L. Liborio, and S. Jackson, Comparison between density functional theory and density functional tight binding approaches for finding the muon stopping site in organic molecular crystals, J. Chem. Phys. **150**, 154301 (2019).

[39] S. B. Zhang and J. E. Northrup, Chemical Potential Dependence of Defect Formation Energies in GaAs: Application to Ga Self-Diffusion, Phys. Rev. Lett. **67**, 2339 (1991).

[40] C. Freysoldt, B. Grabowski, T. Hickel, J. Neugebauer, G. Kresse, A. Janotti, and C. G. Van de Walle, First-principles calculations for point defects in solids, Rev. Mod. Phys. **86**, 253 (2014).

[41] C. Freysoldt, J. Neugebauer, and C. G. Van de Walle, Fully *ab initio* Finite-Size Corrections for Charged-Defect Supercell Calculations, Phys. Rev. Lett. **102**, 016402 (2009).

[42] H.-P. Komsa, T. T. Rantala, and A. Pasquarello, Finite-size supercell correction schemes for charged defect calculations, Phys. Rev. B **86**, 045112 (2012).

[43] Y. Kumagai and F. Oba, Electrostatics-based finite-size corrections for first-principles point defect calculations, Phys. Rev. B **89**, 195205 (2014).

[44] J. P. Perdew, K. Burke, and M. Ernzerhof, Generalized Gradient Approximation Made Simple, Phys. Rev. Lett. **77**, 3865 (1996).

[45] J. Heyd, G. E. Scuseria, and M. Ernzerhof, Hybrid functionals based on a screened Coulomb potential, J. Chem. Phys. **118**, 8207 (2003).

[46] M. E. Bathen, A. Galeckas, J. Coutinho, and L. Vines, Influence of hydrogen implantation on emission from the silicon vacancy in 4*H*-SiC, J. Appl. Phys. **127**, 085701 (2020).

[47] T. Kimoto, A. Itoh, H. Matsunami, S. Sridhara, L. L. Clemen, R. P. Devaty, W. J. Choyke, T. Dalibor, C. Peppermüller, and G. Pensl, Nitrogen donors and deep levels in high-quality 4*H*-SiC epilayers grown by chemical vapor deposition, Appl. Phys. Lett. **67**, 2833 (1995).

[48] W. F. Koehl, B. B. Buckley, F. J. Heremans, G. Calusine, and D. D. Awschalom, Room temperature coherent control of defect spin qubits in silicon carbide, Nature **479**, 84 (2011).

[49] R. Karsthof, M. E. Bathen, A. Galeckas, and L. Vines, Conversion pathways of primary defects by annealing in proton-irradiated *n*-type 4*H*-SiC, arXiv:2007.03985 [cond-mat.mtrl-sci] (2020).

[50] E. Janzén, A. Gali, P. Carlsson, A. Gällström, B. Magnusson, and N. T. Son, The silicon vacancy in SiC, Phys. B: Condens. Matter **404**, 4354 (2009).

[51] V. Ivády, J. Davidsson, N. Tien Son, T. Ohshima, I. A. Abrikosov, and A. Gali, Identification of Si-vacancy related room-temperature qubits in 4*H* silicon carbide, Phys. Rev. B **96**, 161114(R) (2017).

[52] T. Hornos, A. Gali, and B. G. Svensson, Large-scale electronic structure calculations of vacancies in 4*H*-SiC using the Heyd-Scuseria-Ernzerhof screened hybrid density functional, Mater. Sci. Forum **679–680**, 261 (2011).

[53] R. C. Vilão, R. B. L. Vieira, H. V. Alberto, J. M. Gil, and A. Weidinger, Role of the transition state in muon implantation, Phys. Rev. B **96**, 195205 (2017).

[54] R. L. Lichti, W. A. Nussbaum, and K. H. Chow, Hyperfine spectroscopy of muonium in 4*H* and 6*H* silicon carbide, Phys. Rev. B **70**, 165204 (2004).

[55] H. N. Bani-Salameh, Y. G. Celebi, K. H. Chow, B. E. Coss, S. F. J. Cox, and R. L. Lichti, Muonium states and dynamics in 4*H* and 6*H* silicon carbide, Phys. B: Condens. Matter **374–375**, 368 (2006), Proceedings of the Tenth International Conference on Muon Spin Rotation, Relaxation and Resonance.

[56] Y. G. Celebi, R. L. Lichti, B. R. Carroll, P. J. C. King, and S. F. J. Cox, Muonium in 4*H* silicon carbide, Phys. B: Condens. Matter **404**, 5117 (2009).

[57] B. D. Patterson, Muonium states in semiconductors, Rev. Mod. Phys. **60**, 69 (1988).

[58] D. G. Eshchenko, V. G. Storchak, J. H. Brewer, G. D. Morris, S. P. Cottrell, and S. F. J. Cox, Excess electron transport and delayed muonium formation in condensed rare gases, Phys. Rev. B **66**, 035105 (2002).

[59] T. Prokscha, E. Morenzoni, D. G. Eshchenko, N. Garifianov, H. Glückler, R. Khasanov, H. Luetkens, and A. Suter, Formation of Hydrogen Impurity States in Silicon and Insulators at Low Implantation Energies, Phys. Rev. Lett. **98**, 227401 (2007).

[60] Y. G. Celebi, R. L. Lichti, H. N. Bani-Salameh, A. G. Meyer, B. R. Carroll, J. E. Vernon, P. J. C. King, and S. F. J. Cox, Muonium transitions in 4*H* silicon carbide, Phys. B: Condens. Matter **404**, 845 (2009).

[61] G. Henkelman, A. Arnaldsson, and H. Jónsson, A fast and robust algorithm for Bader decomposition of charge density, Comput. Mater. Sci. **36**, 354 (2006).

[62] E. Sanville, S. D. Kenny, R. Smith, and G. Henkelman, Improved grid-based algorithm for Bader charge allocation, J. Comput. Chem. **28**, 899 (2007).

[63] W. Tang, E. Sanville, and G. Henkelman, A grid-based Bader analysis algorithm without lattice bias, J. Phys.: Condens. Matter **21**, 084204 (2009).

[64] M. Yu and D. R. Trinkle, Accurate and efficient algorithm for Bader charge integration, J. Chem. Phys. **134**, 064111 (2011).

[65] G. D. Watkins, in *Advances in Solid State Physics* (Springer, Berlin, 1984), p. 163.

[66] J. P. Goss, R. Jones, S. J. Breuer, P. R. Briddon, and S. Öberg, The Twelve-Line 1.682 eV Luminescence Center in Diamond and the Vacancy-Silicon Complex, Phys. Rev. Lett. **77**, 3041 (1996).

[67] A. Gali, M. Fyta, and E. Kaxiras, *Ab initio* supercell calculations on nitrogen-vacancy center in diamond: Electronic structure and hyperfine tensors, Phys. Rev. B **77**, 155206 (2008).

[68] J. Lento, M. Pesola, J.-L. Mozos, and R. M. Nieminen, Vacancies in SiGe: Jahn-Teller distortion and spin effects, Appl. Phys. Lett. **77**, 232 (2000).